Comparative study of dielectric coating materials for micro-cavity applications

Sidqi, Najwa; Clark, Caspar; Buller, Gerald S.; Thalluri, Gopala Krishna V.V.; Mitrofanov, Jevgenij; Noblet, Yoann

Published in:
Optical Materials Express

DOI:
10.1364/OME.9.003452

Published: 24/07/2019

Document Version
Publisher's PDF, also known as Version of record

Research Article | Vol. 9, No. 8 / 1 August 2019 / Optical Materials Express 3452
Optical Materials EXPRESS

Comparative study of dielectric coating materials for micro-cavity applications

NAJWA SIDQI,[1,2,*] CASPAR CLARK,[1,3] GERALD S. BULLER,[2] GOPALA KRISHNA V. V. THALLURI,[1] JEVGENIJ MITROFANOV,[1,3] AND YOANN NOBLET[1]

[1]Helia Photonics Limited, Rosebank Park, Livingston EH54 7EJ, United Kingdom
[2]Institute of Photonics and Quantum Sciences, School of Engineering and Physical Sciences, Heriot-Watt University, Edinburgh EH14 4AS, United Kingdom
[3]Institute of Thin Films, Sensors and Imaging, University of West of Scotland, Paisley PA12BE, United Kingdom
*ns49@hw.ac.uk

Abstract: We study the potential of common dielectric coating materials used for the fabrication of high reflectance mirrors in micro-cavity devices used in the visible region. We examine materials grown using E-beam and thermal evaporation and magnetron sputtering. The refractive indices and the extinction coefficients of the coatings were calculated from transmission and reflectance spectrophotometric data. The surface roughness of single layer coatings was measured using atomic force microscopy and the scatter of the thin film coatings was approximated from roughness measurements.

1. Introduction

Single-photon technology has been an area of intense research activity for a number of years. While this technology allows sensitive optical measurements to be performed in a wide range of applications such health [1], imaging [2] and biology [3–6], the growing interest in investigating single-photon sources and emitters shown during the past four decades is mainly related to the emergence of quantum communications applications and, in particular, quantum cryptography [7]. Single-photon emission is the emission of one photon resulting from a fluorescence process after a source has been electrically or optically excited by an external power source [8]. However, this emission process suffers from many limitations that prevent it from being used for quantum networking or quantum computing. Usually, the generated photons are emitted isotropically and exhibit a broad energy distribution [9]. These limitations can be addressed by coupling these photon sources to microcavities. A microcavity is an optical resonator allowing the confinement of light in a wavelength-scale dimension in the light propagation direction. Light confinement is achieved in Fabry-Perot microcavities [10] using two different schemes. In the first, confinement is achieved from the internal reflections at the boundaries of two metallic surfaces or dielectric coatings. The second scheme uses the total internal reflections of high reflectance periodic quarter-wave dielectric Bragg reflectors on the scale of the resonant optical wavelength [11] as presented in Fig. 1.

High index dielectric materials frequently used for high reflectance mirrors in the visible region are tantalum pentoxide (Ta_2O_5) [13] and titanium dioxide (TiO_2) [14]. They have been previously developed and characterized for high finesse microcavities [13,15–17] as they have very low optical losses [18]. Combined with silicon dioxide (SiO_2) as a low index dielectric material, these two oxides materials are widely quoted in the literature and two of the most commonly used high index materials for the fabrication of cavities for diamond-based quantum emitters [15]. Another high index dielectric material commonly used in high reflectance mirrors for microcavities is niobium pentoxide(Nb_2O_5) [5,14,19,20] which we previously developed for strongly coupled organic semiconductor and monolayer heterostructures microcavities. Mixing high index pure oxide materials with a proportion of silicon dioxide has demonstrated reduced

#365264 https://doi.org/10.1364/OME.9.003452
Journal © 2019 Received 15 May 2019; revised 3 Jul 2019; accepted 7 Jul 2019; published 24 Jul 2019

Optical Materials EXPRESS

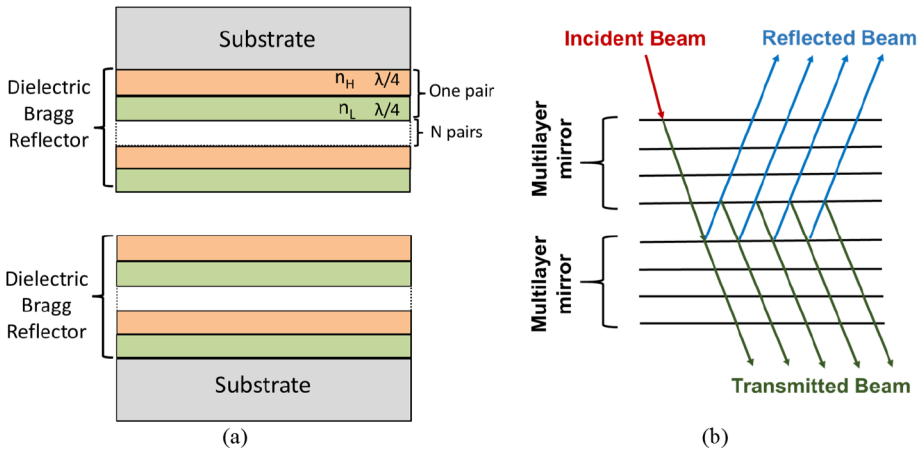

Fig. 1. (a) Structure of Fabry-Perot cavity mirrors. Each mirror is composed of low index/high index dielectric materials pairs. The optical thickness of each layer is a quarter of the emission wavelength of the single photon source. (b) Combined light reflections and transmissions in a multilayer Fabry-Perot cavity, reproduced from [12].

absorption and scatter losses in combinations such as ZrO_2-SiO_2, Nb_2O_5-SiO_2 and TiO_2-SiO_2 films [21,22]. While optical losses for multilayer stacks using these materials have typically been measured as being in the range of ppm for high reflectance coatings in the visible range [21], multilayer stacks are usually produced using Ion Beam Sputtering(IBS) allowing very high packing densities, high refractive indices and greater adhesion properties than multilayers produced by any other deposition methods. Despite all its advantages, IBS has the significant disadvantage of its low deposition rate and therefore its high production cost. With a typical layer deposition rate of a few Ångstroms per minute, growth of a quarterwave multilayer stack for the visible region can take several days. Another major drawback of IBS is being limited to a range of materials, typically metal oxides. In this paper, we present a comparative study of numerous pure low and high index dielectric coatings deposited using classical evaporation and magnetron sputtering methods. In Section 2, we present the materials selected for this study and the deposition methods used for the fabrication of the dielectric coatings. The refractive index n and the extinction coefficient k of the dielectrics are characterized using optical spectrometry in Section 3. The wavelength dependency of the optical constants (n and k) for the coated samples are extracted from the fitted transmission and reflection spectra and the results presented in Sections 3.1–3.2. The surface roughness is measured using Atomic Force Microscopy (Section 4). Measurements of surface roughness are used to estimate optical scatter in the coating.

2. Materials and fabrication methods

Materials and fabrication methods used present the state of art of dielectric materials and commonly used thin film fabrication processes of multilayer dielectric mirrors. There is wide range of deposition methods available including chemical and physical deposition processes. From an industrial and production perspective, we have retained deposition methods that are accessible to the research community, the choice of the deposition method strongly relies on the deposited material and the expected optical properties. The main deposition methods used in this study are: thermal evaporation [23], electron-beam evaporation [23–25] and magnetron sputtering [26]. The studied materials have been selected according to several parameters such as their optical properties (refractive index n and region of transparency), the availability of the deposition method, the toxicity of the materials, and their cost-effectiveness. Other relevant

Optical Materials EXPRESS

parameters such as the chemical and mechanical properties of the coatings (compatibilities with other materials, stoichiometry and intrinsic stresses) have been also decisive in the choice of the dielectric materials to be used in high reflectance coatings for Fabry-Perot cavities.

The thin film materials have been deposited on Corning 2947-75×25 plain 1 mm thick microscope slides, made from soda lime glass. For silicon dioxide coatings, 1 mm thick and 25 mm diameter SF11 witnesses were used instead to allow a greater refractive index contrast during the transmission measurement. The coatings have been deposited from 99.99% purity targets and material sources provided by Scotech Ltd.

Tables 1 and 2 summarize the deposited materials, the deposition methods and the process parameters for each single layer coating. Our results (see Table 3) show that the thickness of the coatings varies around a target value of 500 nm. The thickness results presented in Table 3 have an error below 1%. The thickness of the coating was determined from fitted transmittance and reflectance spectra using the optilayer module of the optichar software. This thickness was chosen so that the single layer coating transmittance and reflectance scans would contain enough interference fringes for the refractive index to be estimated over the spectral region of interest.

Table 1. Source materials and process conditions for thin film low index dielectric coatings.

Material	Method	Source material	Process pressure(mBar)	Deposition rate(Å/s)	Backfill gas(sccm)	Substrate heating(°C)
MgF_2	Thermal evaporation	MgF_2 pellets	2.1×10^{-5} to 6.7×10^{-5}	1	none	100
LiF	Thermal evaporation	LiF_2 pellets	5×10^{-5}	1	none	130
Na_3AlF_6	Thermal evaporation	Cryolite pellets	1.3×10^{-5} to 3.7×10^{-6}	1	none	100
SiO_2	RF Magnetron sputtering	Silicon target	8×10^{-3}	0.34	Ar:20/O_2:6	none
	IAD E-beam	SiO_2 pellets,	9×10^{-5}	2	none	50

Table 2. Source materials and process conditions for thin film high index dielectric coatings.

Material	Method	Source material	Process pressure(mBar)	Deposition rate(Å/s)	Backfill gas(sccm)	Substrate heating (°C)
TiO_2	IAD E-beam P-DC	TiO_2 pellets	1.8×10^{-4}	1	O_2: 35	none
Ta_2O_5	Magnetron sputtering	Ta target	8.8×10^{-3}	1.9	Ar:77 / O_2:45	120
$LaTiO_3$	Reactive E-beam	$LaTiO_3$ pellets	1.3×10^{-2}	3	O_2:10	160
HfO_2	IAD E-beam	Hf pellets	1.2×10^{-4}	1.2	O_2:50	none
Nb_2O_5	Reactive E-beam	Nb pellets	4.4×10^{-4}	1.5	O_2:50	none
ZrO_2	IAD E-beam	Zr tablets	2×10^{-4}	0.8	O_2:50	none
ZnS	Thermal evaporation	ZnS tablets	5×10^{-5} to 2×10^{-5}	1	none	100
ZnSe	Thermal evaporation	ZnSe granules	6×10^{-5} to 4.8×10^{-6}	1	none	100

In Table 1, fluoride materials were deposited using thermal evaporation at a process pressure in the range of 10^{-5}–10^{-6} mBar and a deposition rate of 1 Å/s. At higher evaporation rates, fluorides such as cryolite and magnesium fluoride dissociate, causing a high absorption in the coating [27–29]. For thermally evaporated fluoride coatings, substrate heating was also required to increase the adhesion of the coating to the substrate. Silicon dioxide is deposited using Radio Frequency(RF) magnetron sputtering and Ion Assisted E-beam Deposition (IAD). Use of high energy processes such as sputtering and IAD increase the packing density of the coating and

Optical Materials EXPRESS

Table 3. Summary of the optical constants results for the studied dielectric coatings compared to bulk materials [8, 43–45, 54–58].

Material	Deposition method	d(nm)	n_{1000}	n_{500}	k_{1000}	k_{500}	DF(%)	n_{b1000}	n_{b500}
Ta_2O_5	P-DC Magnetron Sputter	475	2.10	2.15	$<10^{-5}$	$<10^{-5}$	0.3		
TiO_2	IAD E-beam	466	2.27	2.40	$<10^{-5}$	$<10^{-5}$	0.5	2.4856[54]	2.7114[54]
$LaTiO_3$	Reactive E-beam	508	2.04	2.08	$<10^{-5}$	$<10^{-5}$	0.3		
Nb_2O_5	Reactive E-beam	592	2.23	2.31	$<10^{-5}$	$<10^{-5}$	0.3		
HfO_2	IAD E-beam	425	2.04	2.07	$<10^{-5}$	$<10^{-5}$	0.3	2.0833[55]	2.1277[8, 55]
ZrO_2	IAD E-beam	436	2.02	2.08	8×10^{-3}	2×10^{-3}	0.2	2.1248[56]	2.1788[56]
ZnS	Thermal evaporation	527	2.31	2.43	$<10^{-5}$	4×10^{-4}	0.3	2.2925[44]	2.4199[44]
ZnSe	Thermal evaporation	510	2.54	2.77	$<10^{-5}$	2×10^{-2}	0.8	2.4783[45]	2.7326[45]
SiO_2	IAD E-beam	500	1.45	1.47	$<10^{-5}$	5×10^{-4}	0.1	1.4502[57]	1.4619[57]
SiO_2	RF Magnetron Sputter	500	1.45	1.47	$<10^{-5}$	6×10^{-4}	0.1		
LiF	Thermal evaporation	455	1.38	1.39	$<10^{-5}$	$<10^{-5}$	0.1	1.3871[43]	1.3944[43]
MgF_2	Thermal evaporation	530	1.38	1.38	$<10^{-5}$	$<10^{-5}$	0.1	1.3736[58]	1.3798[58]
Cryolite	Thermal evaporation	499	1.40	1.40	7×10^{-4}	5×10^{-3}	0.1		

minimize absorption in the film. RF sputtered silicon dioxide have been deposited from a silicon target in a reactive process environment using (Ar:20 sccm/ O_2: 6 sccm) gas mixture at a rate of 0.34 Å/s; the process pressure was of 8×10^{-3} mBar. IAD silica was evaporated from a SiO_2 source with no oxygen backfill at a deposition rate of 2 Å/s at a process pressure of 10^{-4} mBar. Substrate heating to 50 °C was used as it allowed to achieve a refractive index between 1.47 and 1.45 in the wavelength range 500-1000 nm.

In Table 2, zirconium dioxide, hafnium dioxide and titanium dioxide have been deposited using IAD which increases the optical density of the coatings in comparison to E-beam evaporation. Under low energy evaporation and in the absence of substrate heating, zirconia, hafnia and titania thin films grow with a porous structure and a low packing density. Once the machine is vented, the coatings are vulnerable to air humidity, potentially resulting in changes in the refractive index of the coating. IAD deposition is used in this case to reduce the voids in the coating microstructure which increases the coating packing density and its refractive index. IAD provides a higher kinetic energy allowing the disruption of columnar growth of the coating. For instance, during E-beam evaporation, some atoms hang on the surface of the substrate and trap voids in the coating structure. With ions bombarding the surface of the substrate, the overhanging atoms are displaced leaving the voids open to be filled by the evaporated material. IAD also allows a better oxidation of the deposited film inducing a higher refractive index. Hafnium dioxide, niobium pentoxide and zirconium dioxide have been deposited from metal pellets using IAD E-beam in reactive conditions. An oxygen backfill of 50 sccm was used to establish the stoichiometry of the desired oxides during IAD E-beam evaporation. We chose evaporation from metal sources because the E-beam evaporation from corresponding metal oxides causes a dissociation of the source material and an oxygen deficiency. Substochiometric compositions lead to poor optical properties such as high absorption and low refractive index. Some index inhomogeneity can also appear during the growth of thick layers as the material is consumed from the crucible. Titanium dioxide single layer was also grown using IAD deposition from a titanium dioxide source. By using this deposition method, a refractive index of 2.4-2.5 can be reached even at low substrate temperature [30,31]. The deposition of titanium dioxide is possible from various titanium oxide

Optical Materials EXPRESS

species [31] and the coated film optical constants and microstructure vary considerably with various forms of source material. Starting from a titanium dioxide source, the material vapour mainly dissociates into TiO and TiO_2 species. Supplying a partial oxygen pressure (backfill of 35 sccm) is therefore necessary to overcome any deficit of oxygen in the coating stoichiometry and reduce absorption in the coating. We used a deposition rate of 1 Å/s for IAD deposited titanium dioxide. It has been reported that low deposition rates for E-beam evaporated titania from TiO_2 source allows sufficient time for surface diffusion and reaction with oxygen backfill pressure [32]. Tantalum pentoxide was deposited using pulsed DC(P-DC) magnetron sputtering. This deposition method is characterized by a high energy of sputtered particles allowing to obtain homogeneous coatings and reproducible optical and structural properties [33]. Ta_2O_5 single layer was deposited using (Ar:77 sccm/O_2: 45 sccm) mixture. The oxygen concentration represents nearly 60% in the Ar/O_2 mixture which corresponds to the maximum discharge voltage in the chamber for a proper oxidation of the coating [33,34]. The substrate was heated prior to deposition to 120 °C. Increasing refractive index and coating transmittance with increasing substrate temperature for DC magnetron sputtered tantalum pentoxide coating has been reported in [35] due to the increase of the crystallinity of the coating. ZnS and ZnSe are deposited using thermal evaporation in a pressure range of 10^{-5}-10^{-6} mBar at a deposition rate of 1 Å/s. Use of a low deposition rate reduced material spitting and consequent defects in the coatings structure. For instance, ZnS was deposited from tablets that are hard to melt and the use of a low heating power allows improved control of any spitting from the source. Zinc selenide is generally a difficult material to evaporate, even from a pellet source and suffers from spitting, a low deposition rate is therefore recommended. The substrate is heated at 100 °C in order to promote the adhesion of the coating to the substrate [36].

3. Optical characterisation

The refractive index n and the extinction coefficient k of the dielectric coating represent the real and imaginary components of the complex refractive index η deduced from Maxwell's Equations in an isotropic media [37,38] according to Eq. (1):

$$\eta = n + ik \tag{1}$$

For each single layer, values of the refractive index n, the extinction coefficient k and the thicknesses of the coatings have been extracted from both fitted transmittance and reflectance data using the Optilayer module of the Optichar software, version 5.82 [39,40]. The transmission and reflectance spectra of all thin film coatings were measured in the wavelength range of 350 nm to 2200 nm using a Perkin Elmer Lambda 900 spectrophotometer. We provide a sample of reflectance and transmission spectra for IAD E-beam silicon dioxide and thermally evaporated zinc selenide in respect to the substrate reflectance and transmission in Figs. 2 and 3. A preliminary characterization of microscope slide and SF11 substrates optical constants was also performed based on the spectrometric data and the thickness of the substrates (1 mm) (Figs. 2 and 3).

The measured data are transferred to the Optilayer module. The substrate models were used in the fitting module to identify any coating inhomogeneities.

The refractive index n and the extinction coefficient k of the coatings are respectively fitted by the Cauchy model or normal dispersion and the exponential model described in Eq. (2) [40,41]:

$$n(\lambda) = n_\infty + \frac{A}{\lambda^2} + \frac{B}{\lambda^4}; \mathrm{k}(\lambda) \;=\; \mathrm{B}_0 \exp\left(-\frac{B_1}{\lambda} - B_2\lambda\right) \tag{2}$$

Where n_∞, A and B, B_0, B_1 *and* B_2 are the fitting coefficients of the model.

The Cauchy formula is suitable for materials with a normal dispersion, meaning materials with a monotonous decreasing refractive index for increasing wavelength values.

Optical Materials EXPRESS

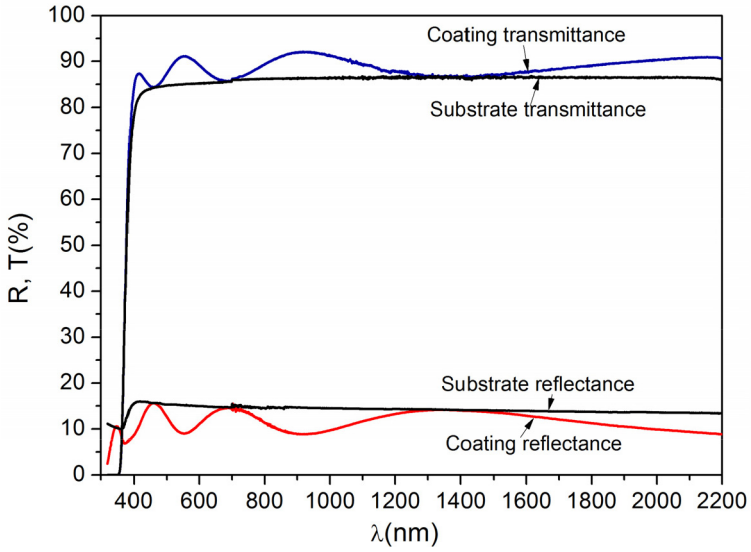

Fig. 2. Measured reflectance and transmission spectra for IAD E-beam silicon dioxide deposited on SF11 substrate using Perkin Elmer Lambda 900 spectrophotometer between 350 nm and 2200 nm.

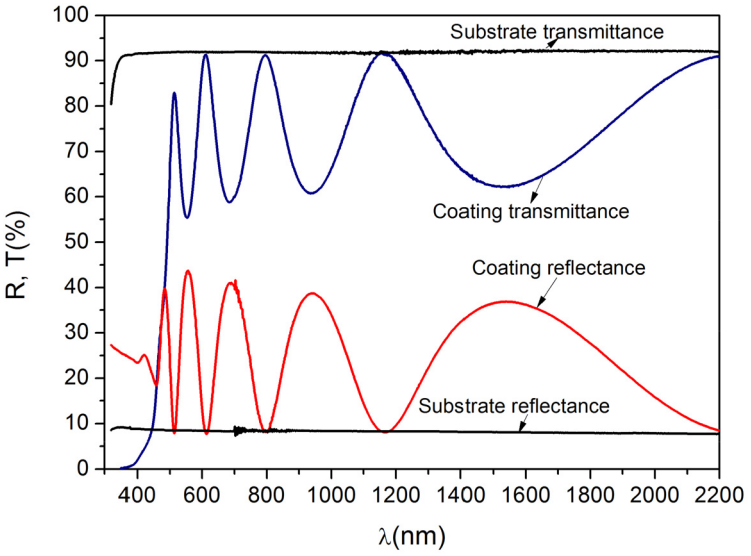

Fig. 3. Measured reflectance and transmission spectra for thermally evaporated zinc selenide deposited on microscope slide substrate using Perkin Elmer Lambda 900 spectrophotometer between 350 nm and 2200 nm.

The closeness between experimental and model data is represented by the discrepancy function DF(see Table 3) as expressed in Eq. (3):

$$DF(X) = \sum_{j=1}^{n} \left(\frac{S(X;\lambda_j) - \widehat{S}(\lambda_j)}{\Delta_j} \right)^2 \tag{3}$$

Optical Materials EXPRESS

Where S is the spectral characteristic of the model, in this case transmittance and reflectance, $\hat{S}$ is the experimentally determined spectral characteristic, λ_j is the wavelength grid in the experimental spectral range, Δ_j are measurement tolerances (typically 1 nm). X is the model vector and its parameters describe the wavelength dependency of both refractive index and extinction coefficient and the coating thickness. The fitting is repeated until the discrepancy function is minimized [41] based on a needle optimization method [42]. For instance, a value of DF of 1 means the deviation of model data from the experimental ones is about 1% across the spectral region of interest. The value of DF is compared to measurement accuracy of the spectrophotometer. Thin film inhomogeneity is checked by manually inputting small linear gradients in film refractive index. According to Perkin Elmer Lambda 900 spectrophotometer specification data, the photometric accuracies for transmittance and reflectance are of 0.05%. We have therefore limited our fitting to discrepancy values above 0.1 in order to avoid overfitting data.

3.1. Refractive index n

The wavelength dependency of the refractive indices is extracted from the fitted reflectance spectra in the wavelength range from 500 nm to 1000 nm. Results for low and high index dielectrics are presented in Figs. 4 and 5.

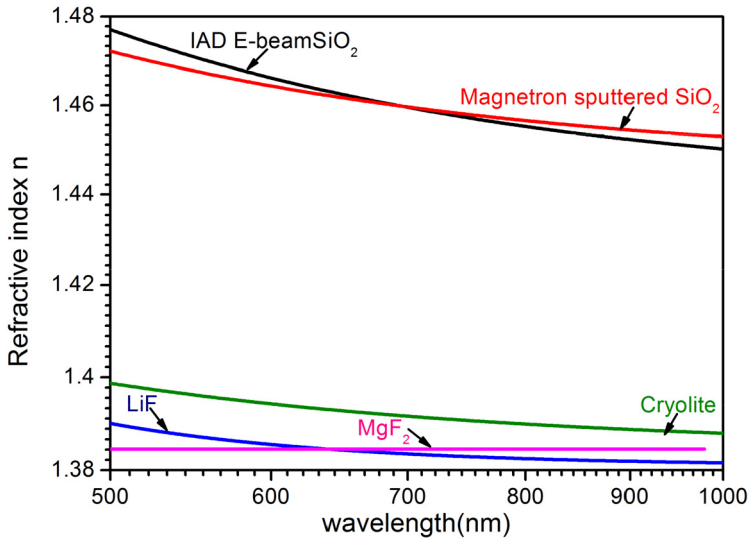

Fig. 4. Refractive index n calculated from fitted reflection data for low index dielectric single layer coatings in the wavelength fitting range 500 nm to 1000 nm.

Thermally evaporated fluorides (lithium fluoride, magnesium fluoride and cryolite) have a low refractive index, ideal for use in high-reflectance structures. Magnesium fluoride and cryolite have refractive indices of 1.385 and 1.399 at 500 nm respectively which show little change over this spectral band. Lithium fluoride refractive index varies between 1.390 at a wavelength of 500 nm and 1.382 at 1000 nm, both of which are very close to accepted reference values reported by Palik [43]. The refractive indices of RF sputtered and IAD E-beam deposited silicon dioxides are very close, especially in the centre of the visible region, and exhibit refractive indices varying between 1.47 at $\lambda = 500$ nm and 1.45 at $\lambda = 1000$ nm.

Thermally evaporated zinc sulphide and zinc selenide have the highest refractive indices of the studied materials. Their refractive indices are also close to bulk values reported in [44] and [45]. Although zinc sulphide is subject to dissociation during evaporation, nearly stochiometric

Optical Materials EXPRESS

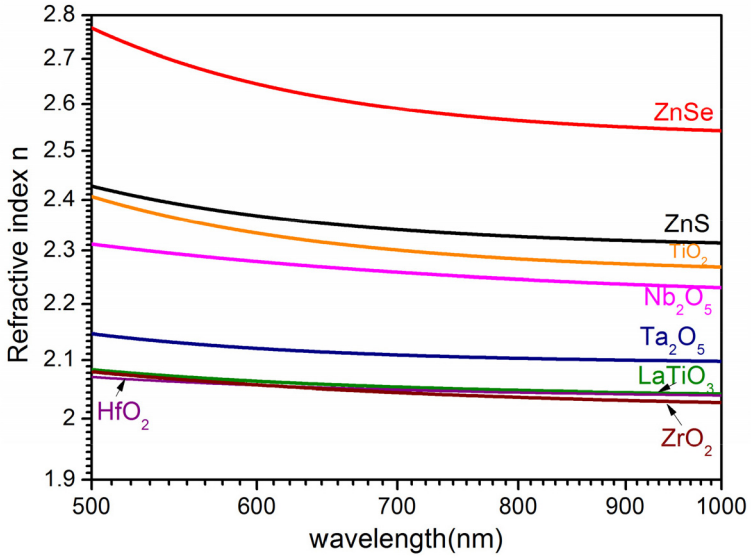

Fig. 5. Refractive index n calculated from fitted reflection data for high index dielectric single layer coatings in the wavelength fitting range 500 nm to 1000 nm.

coatings are still formed as zinc and sulphur recombine near the substrate. The refractive index of zinc sulphide also depends on the substrate temperature [46]. Zinc selenide and zinc sulphide are often found in combination with fluorides in multilayer stacks, for example zinc sulphide and cryolite are a commonly used combination [4748]. For lossless dielectric materials, the ratio in the refractive indices of these high and low index materials can permit a high reflectivity, R, when used in a stack of quarterwave pairs of high and low index materials, as described in Eq. (4) [49].

$$R = \frac{\left(1 - N_R^{2p}\frac{n_H^2}{n_s}\right)^2}{\left(1 + N_R^{2p}\frac{n_H^2}{n_s}\right)^2} \tag{4}$$

Where N_R is the index ratio of the film materials (n_H/n_L), p the number of high/low index quarterwave pairs and n_s is the refractive index of the substrate.

A greater refractive index ratio also widens the bandwidth of the reflectance mirrors as expressed in the following equation [50]:

$$W = \frac{4}{\pi} arcsin\left(\frac{N_R - 1}{N_R + 1}\right) \tag{5}$$

W being the width of the stopband of the quarter wave mirror in wavelength expressed in fractional terms.

IAD E-beam deposited titanium dioxide has the third highest refractive index with a refractive index of 2.40 at 500 nm wavelength. This result is even more outstanding as the grown film was evaporated from a titanium dioxide crucible. Titanium oxide decomposes into suboxides and loses oxygen during E-beam evaporation which can lead to substochiometric compositions. The refractive index distribution of pulsed-DC reactive magnetron sputtered tantalum pentoxide is comparable to refractive index data reported in [33,51] for tantalum pentoxide layers grown using reactive DC magnetron sputtering with similar physical thicknesses. E-beam deposited lanthanum titanate shows a low refractive index dispersion. The coating refractive index varies

Optical Materials EXPRESS

between 2.09 at 500 nm and 2.05 at 1000 nm wavelength. IAD E-beam zirconium dioxide and E-beam hafnium dioxide have very close refractive indices which vary between 2.02 and 2.04 at 500 nm and 2.07 and 2.08 at 1000 nm.

3.2. Extinction coefficient k

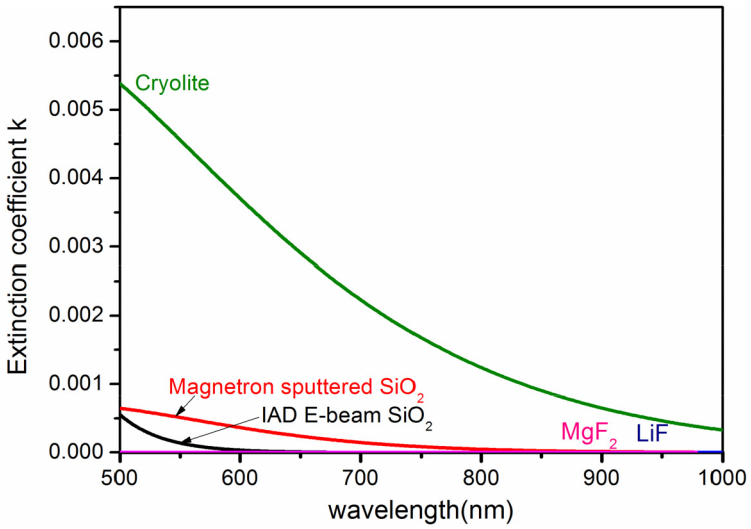

Fig. 6. Extinction coefficient k calculated from fitted transmission data of single layers of low index dielectric materials.

The extinction coefficient k is extracted from the fitted spectral transmission data between wavelengths of 500 nm and 1000 nm and is shown for low and high index materials in Figs. 6 and 7.

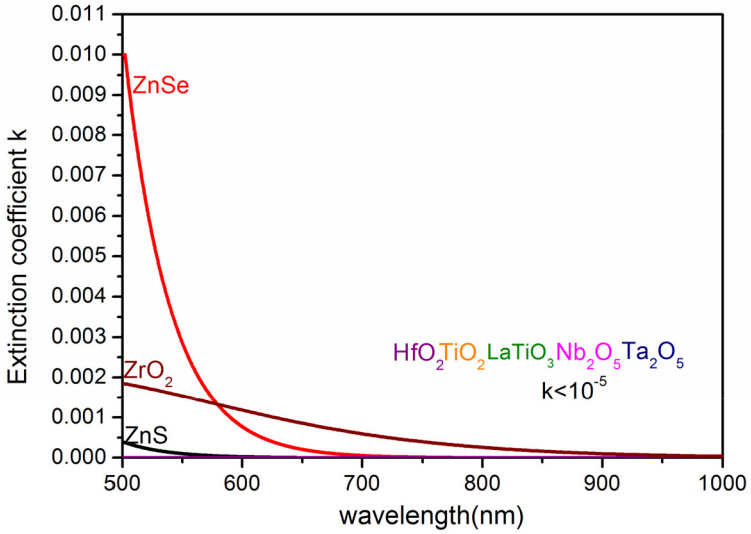

Fig. 7. Extinction coefficient k calculated from fitted transmission data of single layers of high index dielectric materials.

Optical Materials EXPRESS

We report an extinction coefficient k below 10^{-5} for thermally evaporated lithium fluoride and magnesium fluoride. The extinction coefficient k of thermally evaporated cryolite varies between 0.007 at 500 nm to nearly 0.001 at 1000 nm. The optical properties of cryolite are highly dependent on the process temperature and pressure, and a high absorption can be caused by the modification of the chemical composition of the material due to the dissociation of the alumina and the fluoride in the cryolite during the evaporation process. The extinction coefficient of RF sputtered and IAD silicon dioxides is of 6×10^{-3} at 500 nm wavelength. However, the measured absorption of magnetron sputtered silicon dioxide starts at below 750 nm wavelength instead of 550 nm, in the case of IAD E-beam deposition. Fully oxidized silicon dioxide coatings are transparent over the range below 250 nm to at least 3.4 µm. RF sputtered silicon dioxide high absorption can be due to an unbalanced argon to oxygen ratio during the sputtering process.

On the other hand, oxides such as titanium dioxide, tantalum pentoxide, niobium pentoxide and hafnium dioxide and lanthanum titanate have an extinction coefficient below 10^{-5} at wavelengths between 500 nm and 1000 nm. From the same point of view, zinc selenide, zinc sulphide are also suitable for applications beyond 600-700 nm. At 500 nm wavelength, the extinction coefficient k of zinc selenide is equal to 10^{-2}. At a substrate temperature equal to 100 °C, zinc selenide high absorption is explained by the coating low crystallinity [52] which causes a shift of the absorption to shorter wavelengths [53]; the coating absorptance edge is at 2.3 eV which corresponds to about 550 nm. This is also the case for zinc sulphide. However, its extinction coefficient is about one order of magnitude less than zinc selenide.

Making use of the materials and the techniques described in this paper, only few options of low index dielectrics are available, such as magnesium fluoride, lithium fluoride and IAD E-beam evaporated silicon dioxide. This last material can be conveniently used in conjunction with the high index E-beam evaporated refractory metal oxides presented in this study.

3.3. Optical constants summary

Selected values of the estimated optical constants for the dielectric thin film samples are presented in Table 3. Values of the refractive index n_{1000} and n_{500} and the extinction coefficient k_{1000} and k_{500} are given at respective wavelengths of 1000 nm and 500 nm. The physical thickness of the coatings, d, is extracted from the fitted transmission and reflectance spectra. The thickness error is below 1%. The refractive indices at 500 nm and 1000 nm wavelengths are compared to bulk material constants n_{b500} and n_{b1000} from the literature as an indication, assuming stochiometric compositions.

4. Surface roughness

The surface roughness of the deposited materials on microscope slides was evaluated using Atomic Force Microscopy (AFM). All measurements were performed using a Veeco Dimension 3100 AFM system in tapping mode. AFM scans have been performed at a frequency of 0.25 Hz, on a scan area of 1 µm × 1 µm and a sampling matrix of 256 × 256 lines, using Bruker n-doped silicon AFM probe.

The root mean square (RMS) roughness of the studied samples is presented in Table 4. The RMS roughness has been calculated from raw scanning data using the statistical quantities function of Gwyddion software, version 2.51 [59].

We present in the same table an estimation of the scatter in percent at wavelengths of 500 nm and 1000 nm. The scatter S has been calculated from the RMS roughness using Eq. (6) [60] :

$$S = \left(\frac{4\pi r}{\lambda}\right)^2 \tag{6}$$

Where r is the RMS roughness of the coating.

Optical Materials EXPRESS

Table 4. Summary of the Root Mean Square (RMS) roughness values of the studied dielectric coatings and the estimated scatter at 500 nm and 1000 nm from Eq. (6).

Material	Fabrication method	rms roughness (nm)	Scatter(1000 nm) (%)	Scatter(500 nm) (%)
Ta_2O_5	Magnetron Sputter	1.2±0.2	0.02	0.09
TiO_2	IAD E-beam	0.8±0.2	0.01	0.04
$LaTiO_3$	E-beam	3.3±0.4	0.17	0.70
HfO_2	IAD E-beam	3.7+0.2	0.20	0.86
Nb_2O_5	E-beam	1.4±0.3	0.03	0.12
ZrO_2	IAD E-beam	1.5±0.3	0.04	0.14
ZnS	Thermal evaporation	6.8±0.3	0.73	2.92
ZnSe	Thermal evaporation	1.5±0.3	0.04	0.14
SiO_2	IAD E-beam	1.2±0.1	0.02	0.09
SiO_2	Magnetron Sputter	1.7±0.3	0.05	0.18
LiF	Thermal evaporation	4.3±0.2	0.29	1.17
MgF_2	Thermal evaporation	2.9±0.5	0.13	0.53
Na_3AlF_6	Thermal evaporation	1.9±0.6	0.06	0.23
Reference Micro slide/SF11	/	1.0±0.2	0.02	0.06

While most of the thin film coatings deposited on microscope slide show a roughness in the range of 1 nm to 1.5 nm, other coatings such as thermally evaporated zinc sulphide, lithium fluoride, magnesium fluoride, Electron-beam evaporated lanthanum titanate ($LaTiO_3$) and hafnium dioxide exhibit a significantly greater roughness. By contrast, the estimated scatter for titanium dioxide is about 0.04% or 400 ppm at 500 nm. A scatter value of almost 3% for zinc sulphide is not reasonable as it does not agree with the halfwave transmittance loss with respect to the substrate of 0.2 ± 0.05% (Fig. 8). This deviation between the scatter estimated from surface roughness and the optical transmission data is most likely explained by a variation of the rms roughness of the zinc sulphide coating across the large sample area. It is also difficult to perform both rms roughness and transmission measurements in the same spot. Furthermore, the roughness measurement was performed on a few μm⊃2 area whereas transmission measurement is made on many mm⊃2 area. Other measurements, such as total integrated scattering, are a possible route to verify the scatter values presented in Table 4.

For diamond micro-cavity applications, a targeted reflectance of 99.99% at a wavelength of 640 nm is required [61,62]. If we have zero absorption within the multilayer stack, a surface roughness below 3 Å is required to limit the overall optical losses to 0.01%.

A selection of AFM scans for low surface roughness dielectric coatings is provided in Fig. 9. The scans give complementary information about the growth mode and the surface heterogeneity of the coatings. Figure 9 highlights the difference in the surface roughness of thin film single layers for a selection of different materials and growth techniques. For example, both E-beam niobium pentoxide and titanium dioxide (Figs. 9.c and 9.d) show a flat surface with a uniform height while sputtered tantalum pentoxide (Fig. 9.a) shows a flat surface with growing round shaped grains. IAD E-beam deposited zirconium dioxide (Fig. 9.b) exhibits a very dense structure due to the use of an ion gun during the material evaporation. Zinc selenide has a dense and flat microstructure with a grain size between 10 and 15 nm (Fig. 9.e) which is in accordance with values reported in [52] for thermally grown zinc selenide at 100 °C. It has been also demonstrated in [53,63] that smaller grain size induces a shift of the absorption edge to shorter wavelengths. On the other hand, the surface of zinc sulphide appears rougher with a uniform round shape grains ranging from 30 to 50 nm (Fig. 9.f). IAD E-beam silicon dioxide exhibits a very dense structure with a grain size around 20 nm (Fig. 9.g). For RF sputtered silicon dioxide (Fig. 9.h), the film grains are clearly distinguishable and have a round shape with a grain size ranging between 30 to 50 nm. E-beam lanthanum titanate has a flat but uneven surface resulting in a higher surface

Optical Materials EXPRESS

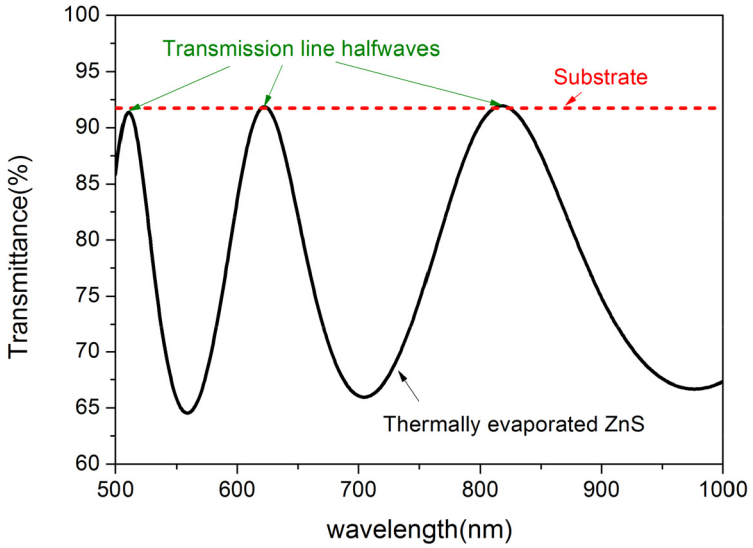

Fig. 8. Halfwaves of thermally evaporated zinc sulphide measured transmittance laying on the substrate transmittance.

roughness (Fig. 9.i). Thermally evaporated magnesium fluoride and cryolite present a similar surface morphology with a flatter surface for thermally evaporated cryolite resulting in a lower surface roughness (Figs. 9.k and 9.l). The two fluorides grow as large islands in a Frank and Vander Merwe like model [64].

Optical Materials EXPRESS

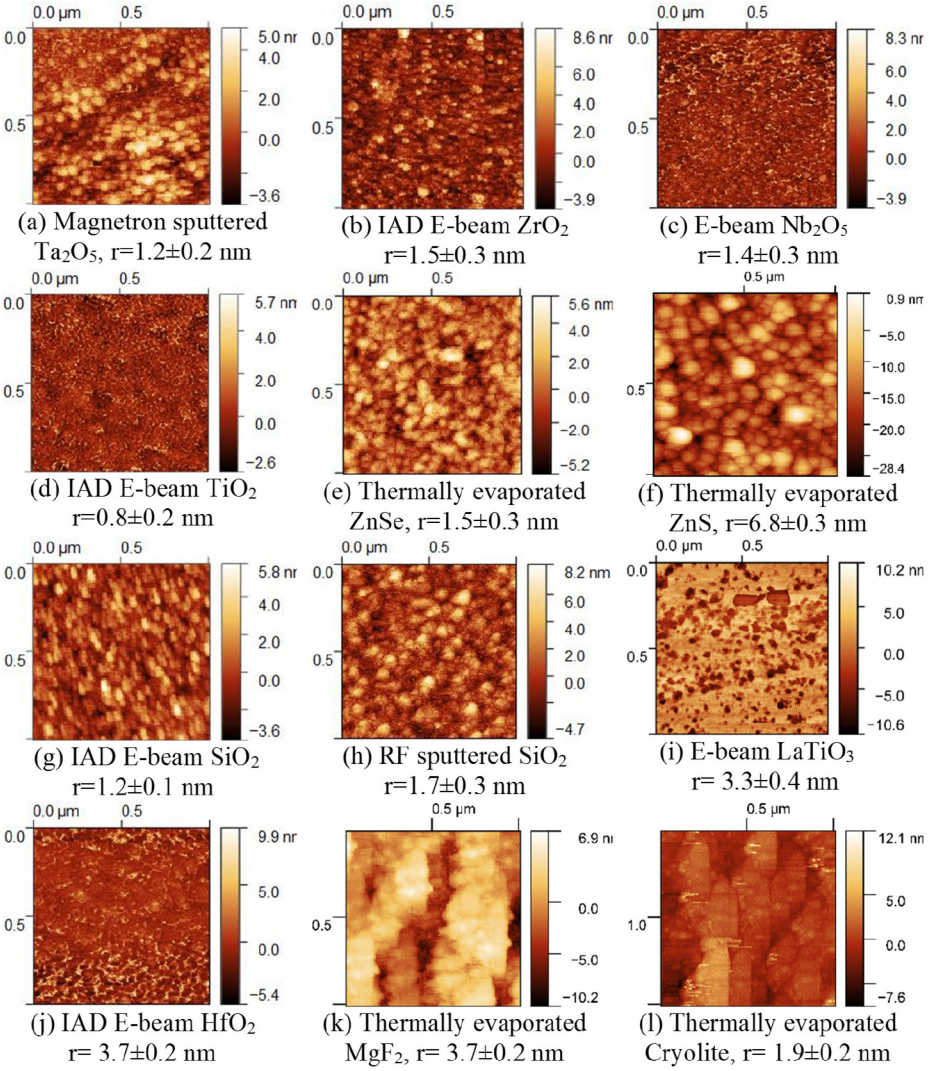

Fig. 9. Selected AFM scans of low roughness coatings deposited on microscope slides with a thickness around 500 nm. The AFM scans have been performed in tapping mode on 1 µm × 1 µm area at a speed of 0.25 Hz using 256 sample/line.

5. Discussion and future works

From this optical characterization, we demonstrated that very low absorption is achieved from pure E-beam evaporated, IAD oxides and thermally evaporated lithium fluoride and magnesium fluoride. We also presented a methodology of determining the optical constants n and k for the thin-film materials studied from spectral transmittance and reflectance data. Based on that, the reflectance, transmittance and absorptance of the quarterwave stack can be calculated at the application wavelength. If we use an IAD E-beam TiO_2/SiO_2 combination at a wavelength of 640 nm with the extinction coefficients extracted for TiO_2 and SiO_2 layers shown in Section 3, a reflectance of 99.99% is attainable for an 11-pair stack ending with a titanium dioxide layer. Other combinations such as IAD E-beam ZrO_2/SiO_2 will require three extra pairs in order to achieve 99.99% reflectance at the same wavelength. However, the deposition of a full stack is

Optical Materials EXPRESS

still feasible within a single day of growth, with the given the deposition rates of the materials and the process base pressure. With a mirror reflectance of 99.99%, we can expect a cavity finesse of around 32 000 from Eq. (7) [11], which fulfills the requirements of most quantum communication micro-cavity source applications.

$$F = \frac{\pi\sqrt{R}}{1-R} \tag{7}$$

A further experimental study will be made to compare the absorption losses for multilayer stacks to the absorptance calculated from the spectral characterization. Many techniques such as the photothermal deflection technique [65], the photothermal common path interferometry [66,67] and lock-in detection [68] allow the accurate measurement of very small absorption losses.

High reflectivity mirrors for quantum communication applications usually require surface roughness between 0.2 nm and 0.3 nm in order to reduce the scatter losses [60]. However, E-beam deposited TiO_2, Ta_2O_5, ZrO_2, Nb_2O_5 and SiO_2 were shown to have a surface roughness between 1 nm and 1.5 nm. Considering a multilayer stack of a similar surface roughness, the total estimated scatter varies between 0.02% and 0.1% at 640 nm wavelength, which reduces the reflectance of the multilayer stack down to 99.9%. Consequently, the finesse of the cavity using these reflective stacks would be reduced to approximately 3200. The scatter of the coatings can be considerably improved in this case by using superpolished substrates as previously demonstrated in [69] for E-beam evaporated Ta_2O_5/SiO_2 multilayer high reflectance coatings. Future experiments will investigate the influence of substrate roughness on the coating roughness using substrates with different polishing grades. However, estimating scatter from surface roughness alone can prove unreliable as seen in the case of zinc sulphide as the rms value may vary on the same sample. Scatter must be therefore measured using other means [70].

The overall optical losses in high reflectance multilayer dielectric coatings are not limited to the absorption and scatter losses intrinsic to the single layers. The reflectance of multilayer coatings is also limited by other parameters such as thermal noise in the multilayer and the substrate driven by the thermal expansion coefficient and the temperature dependence of the refractive index. Thermal noise can be reduced by the use of free standing epitaxial coatings and suitable cavity designs as demonstrated in [71].

Funding

H2020 Marie Skłodowska-Curie Actions (MSCA) Nanoscale solid-state spin systems in emerging quantum technologies Spin-NANO (676108).

Disclosures

The authors declare that there are no conflicts of interest related to this article.

References

1. J. Tsang, J. Kash, and D. Vallett, "Picosecond imaging circuit analysis," IBM J. Res. Dev. **44**(4), 583–603 (2000).
2. J. A. Kash, J. Tsang, D. R. Knebel, and D. P. Vallett, *Non-Invasive Backside Failure Analysis of Integrated Circuits by Time-Dependent Light Emission: Picosecond Imaging Circuit Analysis* (1998), pp. 483–488.
3. T. Isoshima, Y. Isojima, K. Hakomori, K. Kikuchi, K. Nagai, and H. Nakagawa, "Ultrahigh sensitivity single-photon detector using a Si avalanche photodiode for the measurement of ultraweak biochemiluminescence," Rev. Sci. Instrum. **66**(4), 2922–2926 (1995).
4. T. Cookson, K. Georgiou, A. Zasedatelev, R. T. Grant, T. Virgili, M. Cavazzini, F. Galeotti, C. Clark, N. G. Berloff, D. G. Lidzey, and P. G. Lagoudakis, "A Yellow Polariton Condensate in a Dye Filled Microcavity," Adv. Opt. Mater. **5**(18), 1700203 (2017).
5. R. T. Grant, P. Michetti, A. J. Musser, P. Gregoire, T. Virgili, E. Vella, M. Cavazzini, K. Georgiou, F. Galeotti, C. Clark, J. Clark, C. Silva, and D. G. Lidzey, "Efficient Radiative Pumping of Polaritons in a Strongly Coupled Microcavity by a Fluorescent Molecular Dye," Adv. Opt. Mater. **4**(10), 1615–1623 (2016).

Optical Materials EXPRESS

6. M. C. David, S. Niccolo, M. Paolo, C. Caspar, G. L. Pavlos, G. S. Pavlos, and G. L. David, "Polariton-mediated energy transfer between organic dyes in a strongly coupled optical microcavity," Nat. Mater. **13**(7), 712–719 (2014).
7. N. Gisin, G. Ribordy, W. Tittel, and H. Zbinden, "Quantum cryptography," Rev. Mod. Phys. **74**(1), 145–195 (2002).
8. G. S. Buller and R. J. Collins, "Single-photon generation and detection," Meas. Sci. Technol. **21**(1), 012002 (2010).
9. T. Bondo, M. Hennrich, T. Legero, G. Rempe, and A. Kuhn, "Time-resolved and state-selective detection of single freely falling atoms," Opt. Commun. **264**(2), 271–277 (2006).
10. C. Fabry and A. Perot, "Theorie et applications d'une nouvelle méthode de spectroscopie interférentielle," Annales des Chimie et des Physique **7th series**, 115–144 (1899).
11. A. V. Kavokin, J. J. Baumberg, G. Malpuech, and F. P. Laussy, *Microcavities* (Oxford University Press, 2007).
12. H. A. Macleod, "Introduction," in *Thin-film Optical Filters* (CRC Press, 2010), pp. 7–8.
13. S. Reid and I. Martin, "Development of Mirror Coatings for Gravitational Wave Detectors," Coatings **6**(4), 61 (2016).
14. S. K. Rajendran, D. Brida, M. Maiuri, D. Coles, D. Polli, A. M. Adawi, C. Clark, P. Michetti, D. G. Lidzey, G. Cerullo, and T. Virgili, "Ultrafast dynamics of cavity polaritons in an organic semicondutor microcavity," (2012), pp. 1–3.
15. L. Greuter, S. Starosielec, D. Najer, A. Ludwig, L. Duempelmann, D. Rohner, and R. J. Warburton, "A small mode volume tunable microcavity: Development and characterization," Appl. Phys. Lett. **105**(12), 121105 (2014).
16. L. C. Flatten, A. A. P. Trichet, and J. M. Smith, "Spectral engineering of coupled open-access microcavities," Laser Photonics Rev. **10**(2), 257–263 (2016).
17. R. J. Barbour, P. A. Dalgarno, A. Curran, K. M. Nowak, H. J. Baker, D. R. Hall, N. G. Stoltz, P. M. Petroff, and R. J. Warburton, "A tunable microcavity," (2012), pp. 1–2.
18. D. Vander-Hyde, C. Amra, M. Lequime, F. Magaña-Sandoval, J. R. Smith, and M. Zerrad, "Optical scatter of quantum noise filter cavity optics," Classical Quantum Gravity **32**(13), 135019 (2015).
19. S. Dufferwiel, S. Schwarz, F. Withers, A. A. P. Trichet, F. Li, M. Sich, O. D. Pozo-Zamudio, C. Clark, A. Nalitov, D. D. Solnyshkov, G. Malpuech, K. S. Novoselov, J. M. Smith, M. S. Skolnick, D. N. Krizhanovskii, and A. I. Tartakovskii, "Exciton–polaritons in van der Waals heterostructures embedded in tunable microcavities," Nat. Commun. **6**(1), 8579 (2015).
20. D. M. Coles, P. Michetti, C. Clark, W. C. Tsoi, A. M. Adawi, J. S. Kim, and D. G. Lidzey, "Organic Semiconductors: Vibrationally Assisted Polariton-Relaxation Processes in Strongly Coupled Organic-Semiconductor Microcavities," Adv. Funct. Mater. **21**(19), 3690 (2011).
21. S. Chao, W.-H. Wang, and C.-C. Lee, "Low-loss dielectric mirror with ion-beam-sputtered TiO_2–SiO_2 mixed films," Appl. Opt. **40**(13), 2177–2182 (2001).
22. A. Melninkaitis, T. Tolenis, L. Mažule, J. Mirauskas, V. Sirutkaitis, B. Mangote, X. Fu, M. Zerrad, L. Gallais, M. Commandré, S. Kicas, and R. Drazdys, "Characterization of zirconia- and niobia-silica mixture coatings produced by ion-beam sputtering," Appl. Opt. **50**(9), C188–C196 (2011).
23. D. M. Mattox, "Chapter 6 - Vacuum Evaporation and Vacuum Deposition," in *Handbook of Physical Vapor Deposition (PVD) Processing (Second Edition)* (William Andrew Publishing, Boston, 2010), pp. 195–235.
24. D. M. Mattox, "Chapter 9 - Ion Plating and Ion Beam-Assisted Deposition," in *Handbook of Physical Vapor Deposition (PVD) Processing (Second Edition)* (William Andrew Publishing, Boston, 2010), pp. 301–331.
25. J. Bellum, E. Field, D. Kletecka, and L. Finis, "Reactive ion-assisted deposition of e-beam evaporated titanium for high refractive index TiO_2 layers and laser damage resistant, broad bandwidth, high-.(Report)," Appl. Opt. **53**(4), A205 (2014).
26. D. M. Mattox, "Chapter 7 - Physical Sputtering and Sputter Deposition (Sputtering)," in *Handbook of Physical Vapor Deposition (PVD) Processing (Second Edition)* (William Andrew Publishing, Boston, 2010), pp. 237–286.
27. G. Hass and J. B. Ramsey, "Vacuum Deposition of Dielectric and Semiconductor Films by a CO_2 Laser," Appl. Opt. **8**(6), 1115–1118 (1969).
28. H. K. Pulker and C. Zaminer, "Composition and structure of vapour-deposited cryolite films," Thin Solid Films **5**(5-6), 421–428 (1970).
29. R. P. Netterfield, "Refractive indices of zinc sulfide and cryolite in multilayer stacks," Appl. Opt. **15**(8), 1969–1973 (1976).
30. J. M. Bennett, E. Pelletier, G. Albrand, J. P. Borgogno, B. Lazarides, C. K. Carniglia, R. A. Schmell, T. H. Allen, T. Tuttle-Hart, K. H. Guenther, and A. Saxer, "Comparison of the properties of titanium dioxide films prepared byvarious techniques," Appl. Opt. **28**(16), 3303–3317 (1989).
31. H. Selhofer, E. Ritter, and R. Linsbod, "Properties of titanium dioxide films prepared by reactive electron-beam evaporation from various starting materials," Appl. Opt. **41**(4), 756–762 (2002).
32. H. W. Lehmann and K. Frick, "Optimizing deposition parameters of electron beam evaporated TiO_2 films," Appl. Opt. **27**(23), 4920–4924 (1988).
33. O. D. Vol'pyan, P. P. Yakovlev, B. B. Meshkov, and Y. A. Obod, "Optical properties of Ta_2O_5 films obtained by reactive magnetron sputtering," J. Opt. Technol. **70**(9), 669–672 (2003).
34. S. Schiller, U. Heisig, K. Steinfelder, and J. Strümpfel, "Reactive D.C. sputtering with the magnetron-plasmatron for tantalum pentoxide and titanium dioxide films," Thin Solid Films **63**(2), 369–375 (1979).
35. S. V. J. Chandra, S. Uthanna, and G. M. Rao, "Effects of substrate temperature on properties of pulsed dc reactively sputtered tantalum oxide films," Appl. Surf. Sci. **254**(7), 1953–1960 (2008).
36. E. Ritter and R. Hoffmann, "Influence of Substrate Temperature on the Condensation of Vacuum Evaporated Films of MgF_2 and ZnS," J. Vac. Sci. Technol. **6**(4), 733–736 (1969).

Optical Materials EXPRESS

37. J. C. Maxwell, "On physical lines of force," The London, Edinburgh and Dublin Philosophical Magazine and Journal of Science **4th series**, 161–175, 282–291, 338–349, 113–124, 185–195 (1861).
38. M. Born and E. Wolf, *Principles of Optics: Electromagnetic Theory of Propagation, Interference and Diffraction of Light ed 7* (Cambridge University Press, 2002).
39. M. K. Trubetskov and A. V. Tikhonravov, "OptiLayer Thin film Software," (OptiLayer GmbH).
40. T. Amotchkina, M. Trubetskov, A. Tikhonravov, I. B. Angelov, and V. Pervak, "Reliable optical characterization of e-beam evaporated TiO_2 films deposited at different substrate temperatures," Appl. Opt. **53**(4), A8–A15 (2014).
41. A. V. Tikhonravov, M. K. Trubetskov, T. V. Amotchkina, G. DeBell, V. Pervak, A. K. Sytchkova, M. L. Grilli, and D. Ristau, "Optical parameters of oxide films typically used in optical coating production," Appl. Opt. **50**(9), C75–C85 (2011).
42. A. V. Tikhonravov and M. K. Trubetskov, "Development of the needle optimization technique and new features of OptiLayer design software," in *International Symposium on Optical Interference Coatings*, (SPIE, 1994).
43. E. D. Palik and W. R. Hunter, "Lithium Fluoride (LiF)," in *Handbook of Optical Constants of Solids*, E. D. Palik, ed. (Academic Press, 1985), pp. 675–693.
44. C. A. Klein, "Room-temperature dispersion equations for cubic zinc sulfide," Appl. Opt. **25**(12), 1873–1875 (1986).
45. B. Tatian, "Fitting refractive-index data with the Sellmeier dispersion formula," Appl. Opt. **23**(24), 4477–4485 (1984).
46. D. Kurbatov, A. Opanasyuk, and H. Khlyap, "Substrate-temperature effect on the microstructural and optical properties of ZnS thin films obtained by close-spaced vacuum sublimation," Phys. Status Solidi A **206**(7), 1549–1557 (2009).
47. A. E. Ennos, "Stresses Developed in Optical Film Coatings," Appl. Opt. **5**(1), 51–61 (1966).
48. M. Banning, "Practical Methods of Making and Using Multilayer Filters," J. Opt. Soc. Am. **37**(10), 792 (1947).
49. H. A. Macleod, "Multilayer high-reflectance coatings," in *Thin-film Optical Filters* (CRC Press, 2010), p. 216.
50. H. A. Macleod, "Multilayer high-reflectance coatings," in *Thin-film Optical Filters* (CRC Press, 2010), p. 222.
51. K. Zhang, R. E. D. T. M. Faber, and D. Ristau, "Plasma Assisted Pulsed DC Magnetron Sputtering System for Optical Thin Film Coatings," in *Optical Interference Coatings*, OSA Technical Digest (online) (Optical Society of America, 2013), ThB.6.
52. S. Chaliha, M. N. Borah, P. C. Sarmah, and A. Rahman, "Effect of substrate temperature on structural properties of thermally evaporated ZnSe thin films of different thickness," J. Phys.: Conf. Ser. **114**, 012048 (2008).
53. M. R. A. Bhuiyan, A. H. Miah, and J. Begum, *Substrate Temperature Effect on the Structural and Optical Properties of ZnSe Thin Films* (2012), Vol. 36, pp. 233–240.
54. J. R. DeVore, "Refractive Indices of Rutile and Sphalerite," J. Opt. Soc. Am. **41**(6), 416–419 (1951).
55. D. L. Wood, K. Nassau, T. Y. Kometani, and D. L. Nash, "Optical properties of cubic hafnia stabilized with yttria," Appl. Opt. **29**(4), 604–607 (1990).
56. D. L. Wood and K. Nassau, "Refractive index of cubic zirconia stabilized with yttria," Appl. Opt. **21**(16), 2978–2981 (1982).
57. H. R. Philipp, "Silicon Dioxide (SiO_2) (Glass)," in *Handbook of Optical Constants of Solids*, E. D. Palik, ed. (Academic Press, 1985), pp. 749–763.
58. M. J. Dodge, "Refractive properties of magnesium fluoride," Appl. Opt. **23**(12), 1980–1985 (1984).
59. D. Nečas and P. Klapetek, "Gwyddion, Free SPM data analysis software."
60. T. Klaassen, M. P. van Exter, and J. P. Woerdman, "Characterization of scattering in an optical Fabry-Perot resonator," Appl. Opt. **46**(22), 5210 (2007).
61. S. Bogdanovic, S. B. van Dam, C. Bonato, L. C. Coenen, A. Zwerver, B. Hensen, M. Liddy, T. Fink, A. Reiserer, M. Loncar, and R. Hanson, "Design and low-temperature characterization of a tunable microcavity for diamond-based quantum networks," Appl. Phys. Lett. **110**(17), 171103 (2017).
62. D. Riedel, I. Söllner, B. J. Shields, S. Starosielec, P. Appel, E. Neu, P. Maletinsky, and R. J. Warburton, "Deterministic enhancement of coherent photon generation from a Nitrogen-Vacancy center in ultrapure diamond," Phys. Rev. X **7**(3), 031040 (2017).
63. A. Kathalingam, T. Mahalingam, and C. Sanjeeviraja, "Optical and structural study of electrodeposited zinc selenide thin films," Mater. Chem. Phys. **106**(2-3), 215–221 (2007).
64. E. Alfonso, J. Olaya, and G. Cubillos, "Thin Film Growth Through Sputtering Technique and Its Applications," in *Crystallization - Science and Technology* (2012).
65. J. Sancho-Parramon, J. Ferré-Borrull, S. Bosch, A. Krasilnikova, and J. Bulir, "New calibration method for UV–VIS photothermal deflection spectroscopy set-up," Appl. Surf. Sci. **253**(1), 158–162 (2006).
66. L. Anghinolfi, M. Prato, A. Chtanov, M. Gross, A. Chincarini, M. Neri, G. Gemme, and M. Canepa, "Optical properties of uniform, porous, amorphous Ta_2O_5 coatings on silica: temperature effects," J. Phys. D: Appl. Phys. **46**(45), 455301 (2013).
67. C. Clark, R. Bassiri, I. Martin, A. Markosyan, P. G. Murray, D. Gibson, S. Rowan, and M. M. Fejer, "Comparison of single-layer and double-layer anti-reflection coatings using laser-induced damage threshold and photothermal common-path interferometry," Coatings **6**(2), 20 (2016).
68. H. Waechter, D. Munzke, A. Jang, and H.-P. Loock, "Simultaneous and Continuous Multiple Wavelength Absorption Spectroscopy on Nanoliter Volumes Based on Frequency-Division Multiplexing Fiber-Loop Cavity Ring-Down Spectroscopy," Anal. Chem. **83**(7), 2719–2725 (2011).

Optical Materials EXPRESS

69. S. E. Watkins, J. P. Black, and B. J. Pond, "Optical scatter characteristics of high-reflectance dielectric coatings and fused-silica substrates," Appl. Opt. **32**(28), 5511–5518 (1993).
70. G. Harry, T. P. Bodiya, and R. DeSalvo, "Optical scatter," in *Optical Coatings and Thermal Noise in Precision Measurement* (Cambridge University Press, 2012), p. 168.
71. D. C. Garrett, Z. Wei, J. M. Michael, Y. Jun, and A. Markus, "Tenfold reduction of Brownian noise in high-reflectivity optical coatings," Nat. Photonics **7**(8), 644–650 (2013).